Shape sensing of NREL 5 MW offshore wind turbine blade using iFEM methodology

Mingyang Li [a,b], Yildirim Dirik [b], Erkan Oterkus [b,*], Selda Oterkus [b]

[a] Ocean College, Jiangsu University of Science and Technology, Zhenjiang, China
[b] Department of Naval Architecture, Ocean and Marine Engineering, University of Strathclyde, Glasgow, United Kingdom

ARTICLE INFO

ABSTRACT

In this study, the shape sensing of a blade of the NREL 5 MW offshore wind turbine is presented by using the inverse Finite Element Method (iFEM) under real loading conditions. Among the applied forces, the aerodynamic forces are calculated based on the Blade Element Momentum Theory (BEMT). The results of iFEM with full sensors and reduced sensors are compared with the reference Finite Element Method (FEM) analysis to test the accuracy of the iFEM analysis. The practical distribution of the iFEM elements with sensors is explored and the effects of different wind velocities are investigated to make the analysis more practical. Based on numerical results, it is concluded that iFEM is a suitable technique for shape sensing of offshore wind turbines.

1. Introduction

Composite materials have been widely utilized to manufacture critical structures in engineering fields. For the offshore industry, the blade of the offshore wind turbines (OWTs) is generally made of fiber-reinforced composites. Nowadays, the blade is usually over 40 m long and consists of two outer surfaces and shear webs (Kim et al., 2019). The shear webs are designed and applied to increase the strength and reduce the weight of the blade. All of the components are generally fabricated by glass/carbon fiber composites. Concerning traditional materials that are used for offshore installations such as stainless steel, composite materials can fulfill the requirements of larger blades with lower weights. At the same time, it can also provide enough strength for the blade. The blade is exposed to strong wind environments. Besides, there are also other additional types of loads such as centrifugal force acting on the blade. Therefore, the blades usually experience large structural deformations and this can result in fatigue or damage problems. It is reported that the damage for an OWT, usually occurs at the tower, the rotor, and the blade regions (Ciang et al., 2008), and it may be necessary to replace the blades (Swartz et al., 2010). If the blades cannot be kept in service, the OWT will suffer a long period of downtime and then financial losses (Antoniadou et al., 2015). Additionally, the OWTs are usually located away from the shore and blades are much higher than the water surface, which means that they are not easy to access. It is very difficult to perform the inspection and maintenance of the blade.

Lacking the lifting equipment will also make the situation more severe. In order to reduce downtime and enhance the performance of the OWT, it is quite necessary to apply the structure health monitoring (SHM) system to the blade to monitor the safety condition of the blade.

The process of SHM can be simply summarized as first collecting the data from the relevant structure and then transmitting the information to the SHM system (Hsu et al., 2014). After analyzing the collected data, the health condition of the structure can be obtained. The basic requirements for the SHM system are, on one hand, to provide reliable and robust information concerning the structural condition, and on the other hand, the process should be fast enough for real-time monitoring. With the help of the SHM system, the OWT not only can be safer and more profitable by reducing the possibility of sudden breakdown and then the cost of maintenance but also beneficial for future design and development (Hsu et al., 2014; Yang et al., 2014). For the blade of OWTs, there are mainly three kinds of SHM methods widely used which are the acoustic emission (AE) method, vibration-based method, and strain-based method. According to Schubel et al. (2013), the most promising methods for continuous offshore monitoring would be AE and strain-based methods. However, the AE method is confined to the field of damage detection. For the strain-based method, Fibre Bragg Grating (FBG) technology is considered one of the key sensing technologies.

FBG technology has been developed since the 1990s and it achieves data acquisition by broadband lights (Ciang et al., 2008). These lights have their wavelength and their frequency change along with the

* Corresponding author.
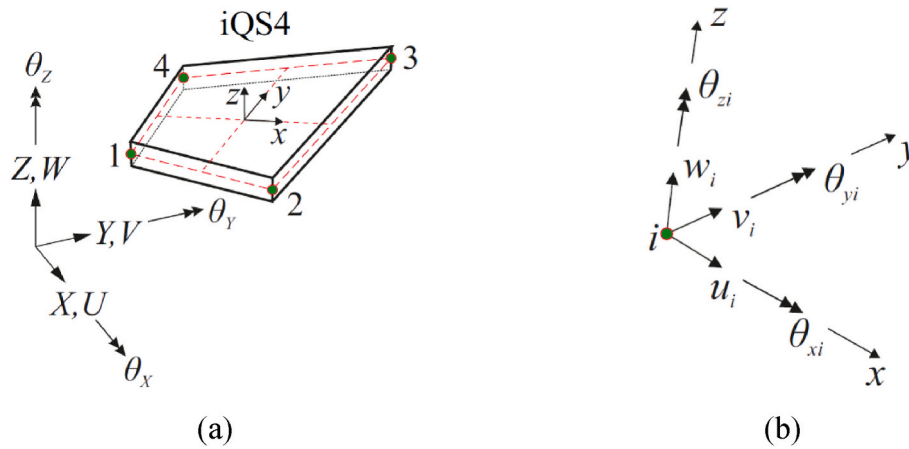 *E-mail address:* erkan.oterkus@strath.ac.uk (E. Oterkus).

Fig. 1. (a) iQS4 element with the local coordinate system (LCS) (*x,y,z*) at the central plane and global coordinate system (GCS) (*X, Y, Z*) of the structure (b) the total 6 DOFs (*U,V,W*, θ_x, θ_y, θ_z) of iQS4 element in its LCS (Kefal et al., 2016).

collected data and by separating the frequency interval, the strain data which contains the real-time information of the structure can be obtained (Joosse et al., 2002). With respect to conventional strain gauges, FBG sensors have plenty of advantages. First of all, they have lower weights and smaller sizes. Then, they are suitable for long-distance signal transmission with less loss. Last but not least, they are less affected by harsh environments (Ciang et al., 2008; Joosse et al., 2002; Arsenault et al., 2013). For the SHM of the blade of OWTs, two main features should be highlighted. On one hand, one FBG cable can contain multiple sensors and the number of sensors can reach 100. On the other hand, due to their small size, FBG sensors can be installed inside the composite materials without influencing the properties (Ciang et al., 2008; Joosse et al., 2002; Arsenault et al., 2013). The SHM system will benefit from these two characteristics and they will reduce the required number of sensors and make the whole system more cost-effective. Currently, FBG sensors have already been used for the structural monitoring of blades. Arsenault et al. (2013) focused on the distribution of the sensors on the blade and they tested their arrangement of sensor placement under various static and dynamic loading conditions. No matter the static case or the dynamic cases, their results matched well with the reference. Kim et al. (2013) used FBG sensors to monitor the deflections of the blade. The FBG sensors were embedded in the composite materials located in the zones between the web and the cap. The high accuracy of this type of distribution was verified through experimental procedure after comparisons against the results from electrical strain gauges (ESGs) and theoretical FEM analysis. Damage estimation by FBG sensors was also explored by Tian et al. and they gave their attention to a 13.2 m blade under static loads. By combing the Chi-Square distribution (CSD) theory and the feature information fusion (FIF) theory, the location of the damage can be detected (Tian et al., 2015).

Apart from sensing technology, interpretation methodology would be another critical aspect of SHM systems (Joosse et al., 2002). In order to perform the three-dimensional displacement monitoring (shape sensing) of a blade in real-time, iFEM can be a suitable alternative. iFEM was developed by Tessler and Spanger in 2003 (Tessler and Spanger, 2003). After about two decades of development, nowadays, there are a variety of elements have been developed including beam (Gherlone et al., 2012, 2014), shell (Tessler and Spanger, 2004; Kefal et al., 2016), and solid elements (Fachinotti et al., 2008, 2015). For the application of iFEM to the blade, Albanesi et al. (2017) used a kind of shell element that is degenerated from a three-dimensional solid element to perform the iFEM analysis of a 440 kW wind turbine. The thick composite blade structure is successfully modeled by their elements and the blade is analyzed under both aerodynamic and inertial loadings. Nevertheless, they just focused on using the iFEM method to improve the performance

of the orthotropic composite materials (Albanesi et al., 2017, 2018), and SHM is not mentioned in their research for the selection of the sensor locations for the practical application of iFEM to the blade. Kefal et al. (Cerracchio et al., 2015; Kefal et al., 2017) generated a three-node inverse element, i3-RZT, for sandwich plates based on the Refined Zigzag Theory (RZT). The accuracy of this element was verified through two examples. Furthermore, Kefal and Yildiz (2017) then applied this element to a wing-shaped structure and three loading conditions (bending, torsion, and membrane) were considered. The practical distribution of sensors was explored and it was concluded that, even with a small number of sparsely distributed FBG sensors, the deformation condition of the wing can be monitored.

For this study, attention will be given to the iFEM analysis of the NREL 5 MW turbine blade using the iQS4 element (Kefal et al., 2016). iQS4 element is a quadrilateral element and compared to other types of shell elements (including i3-RZT), it is simpler to be used. Quadrilateral elements have the advantage of being highly accurate. iQS4 has been used in the marine and offshore fields successfully and its robustness and accuracy have been demonstrated (Kefal and Oterkus, 2016a, 2016b; Kefal et al., 2018; Li et al., 2019). Moreover, the iQS4 element has shown the potential for damage/crack detection on the basis of recent research studies (Colombo et al., 2019; Li et al., 2020) and it will make iQS4 elements more suitable for the monitoring of the blade. In addition, the iQS4 element can be used for the majority of offshore installations, so applying it to the blade will contribute to generating a SHM system for the whole OWTs. In this study, only shape sensing of the SHM process is considered which is a critical component of the SHM process. This paper will be divided into the following parts: the basic theory and fundamental equations of the iFEM/iQS4 element will briefly be introduced in Section 2. Then, Section 3 will present the numerical analysis. Three different types of forces will be taken into consideration and three groups of analysis will be performed after the model generation and force calculation steps. The first analysis is given in Section 3.3 to determine the reasonable mesh size for the iFEM model. Then the analysis for both static (Section 3.4) and dynamic (Section 3.5) cases will be performed and the effects of various wind velocities will be explored. Finally, a summarized conclusion will be given. To the best of the authors' knowledge, it is the first time to use the iQS4 element to perform shape sensing of the composite blade of the OWT under practical loading conditions.

2. Formulation of iQS4 element

2.1. iFEM methodology

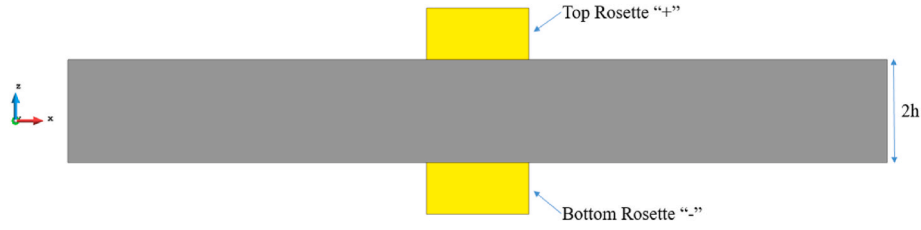iFEM formulation is mainly based on defining a function represent-

Fig. 2. Strain data collection for iQS4 element from both surfaces of the structure.

ing the difference between measured and numerical strain values which can be written as:

$$\varphi_e(u^e) = w_m \|e(u^e) - e^*\| + w_b \|k(u^e) - k^*\| + w_s \|\gamma(u^e) - \gamma^*\| \tag{1}$$

where $e(u^e)$, $k(u^e)$, and $\gamma(u^e)$ are the vectors containing the numerical membrane, bending, and transverse shear strains, respectively, whereas e^*, k^*, and γ^* are the corresponding measured values. w_m, w_b, and w_s are the weighting constants for the membrane, bending, and transverse shear behaviors. In general, if the strain data is available, the values of these three constants are specified as 1. In contrast, if the experimental strains are not provided for the iFEM elements, a small number (10^{-4}) is recommended as the weighting constant for these elements. By doing so, the continuity of the analysis can be ensured. The selection of the weighting constants can be flexible and they can be decided based on the real condition of the application.

iFEM is aiming to minimize the differences between the experimental strains and numerical strains. Therefore, the functional $\varphi_e(u^e)$ is differentiated against the nodal displacement as:

$$\frac{\partial \varphi_e(u^e)}{\partial u^e} = 0 \tag{2a}$$

and finally, the following equation can be obtained:

$$K^e u^e = F^e \tag{2b}$$

where k^e is made of shape functions and it will be constant unless the boundary conditions change during the analysis. It means that during the whole iFEM process, no matter how the loading conditions vary, only the input matrix F^e, formed by strain measurements, is going to be updated, which allows the analysis to be performed in real-time.

2.2. iQS4 element

iQS4 element is a 4-node quadrilateral shell element (Fig. 1) with a thickness of $2h$. "$z = +h$" represents the top surface of the iQS4 element and "$z = -h$" represents the bottom surface. For each node of the iQS4 element, there are 6 degrees of freedom (DOFs) (U, V, W, θ_x, θ_y, θ_z), i.e. there are 24 DOFs for each iQS4 element in total. Compared with other types of iFEM shell elements, the iQS4 element takes the drilling rotation into consideration and this contributes to the avoidance of the shear-locking phenomenon (Kefal et al., 2016). The relationship between the components of the strain matrix and the nodal displacements can be linked by shape functions B_m, B_b, and B_s which are a combination of linear/quadratic shape functions describing the membrane, bending, and transverse shear behaviors, respectively. The detailed expressions of these shape functions can be found in (Kefal et al., 2016; Kefal, 2017). Then, the numerical strains of each element can be obtained by considering the first-order shear deformation theory (FSDT) as:

$$\begin{Bmatrix} \varepsilon_{xx} \\ \varepsilon_{yy} \\ \gamma_{xy} \end{Bmatrix}^e = e(u^e) + zk(u^e) = B_m u^e + zB_b u^e \tag{3a}$$

$$\begin{Bmatrix} \gamma_{xz} \\ \gamma_{yz} \end{Bmatrix}^e = \gamma(u^e) = B_s u^e \tag{3b}$$

2.3. Strain data collection

For the application of iFEM, the sensors are installed on both surfaces of the shell structure (Fig. 2) and the sensors collect the required strain data from the top " + " and bottom " − " surfaces. After obtaining the experimental strain data, the in situ membrane strains and in situ bending curvatures can be calculated on the basis of the following equations:

$$[e]^i = \begin{Bmatrix} e_1 \\ e_2 \\ e_3 \end{Bmatrix}^i = \frac{1}{2} \begin{Bmatrix} \varepsilon_{xx}^+ + \varepsilon_{xx}^- \\ \varepsilon_{yy}^+ + \varepsilon_{yy}^- \\ \gamma_{xy}^+ + \gamma_{xy}^- \end{Bmatrix}^i \quad (i = 1...n) \tag{4a}$$

$$[k]^i = \begin{Bmatrix} k_1 \\ k_2 \\ k_3 \end{Bmatrix}^i = \frac{1}{2h} \begin{Bmatrix} \varepsilon_{xx}^+ - \varepsilon_{xx}^- \\ \varepsilon_{yy}^+ - \varepsilon_{yy}^- \\ \gamma_{xy}^+ - \gamma_{xy}^- \end{Bmatrix}^i \quad (i = 1...n) \tag{4b}$$

where n represents the number of sensors. The transverse shear strains cannot be obtained from the experimental measurements. However, for most marine and offshore applications, the structures can be treated as "thinshell" and the plane-stress condition can be utilized. Therefore, the transverse shear strains can be neglected and there will be no impact on the iFEM analysis. In this study, FEM is utilized to generate "synthetic" strain data to be used as input for iFEM analysis. FEM analysis can also play an important role in determining the critical regions of the structure, which can guide the selection of the sensor locations.

2.4. Post-processing for iFEM analysis

After performing the iFEM analysis, the full-field deformations of the structure can be calculated. By utilizing displacements and rotations, strain and stress distributions can be obtained.

3. Numerical results

3.1. Model generation

In order to generate the model of the blades of offshore wind turbines, the typical and widely used NREL 5 MW offshore wind turbine was selected. It has 3 blades with a diameter of 123 m and these blades are installed to a hub, which is located 90 m above the water surface, and its diameter is 3 m. The pre-cone angle (θ_c) is 2.5°. However, in order to simplify the problem, the tilt angle was ignored. Additional information about this offshore wind turbine can be found in (Jonkman et al., 2009). An open-access software- NuMAD was utilized to create the model of a single blade. NuMAD was developed by Sandia National Laboratories and it was specifically created to reduce the difficulties of three-dimensional blade model generation (Berg and Resor, 2012). The accuracy of this software has been proved and it has been widely used for FEM analysis of blades (Berg and Resor, 2012; Resor, 2013; Zhang et al., 2018; Yang and Baeder, 2016; Fernandez et al., 2018). For the current analysis, due to the fact that NuMAD can generate some input files which can be used by ANSYS software directly, ANSYS was used for

Table 1
The parameters of the blade.

| Section Number	Blade Span (m)	Twist Angle (deg)	Chord Length (m)	Airfoil Table
1	0.00E+00	1.33E+01	3.3860E+00	Cylinder 1
2	1.37E+00	1.33E+01	3.3860E+00	
3	4.10E+00	1.33E+01	3.8540E+00	
4	6.83E+00	1.33E+01	4.1670E+00	Cylinder 2
5	1.03E+01	1.33E+01	4.5570E+00	DU99-W-405
6	1.44E+01	1.15E+01	4.6520E+00	DU99-W-350
7	1.85E+01	1.02E+01	4.4580E+00	
8	2.26E+01	9.01E+00	4.2490E+00	DU97-W-300
9	2.67E+01	7.80E+00	4.0070E+00	DU91-E−250
10	3.08E+01	6.54E+00	3.7480E+00	
11	3.49E+01	5.36E+00	3.5020E+00	DU93-W-210
12	3.90E+01	4.19E+00	3.2560E+00	
13	4.31E+01	3.13E+00	3.0100E+00	NACA-64-618
14	4.72E+01	2.32E+00	2.7640E+00	
15	5.13E+01	1.53E+00	2.5180E+00	
16	5.47E+01	8.63E-01	2.3130E+00	
17	5.74E+01	3.70E-01	2.0860E+00	
18	6.01E+01	1.06E-01	1.4190E+00	
19	6.15E+01	0.00E+00	1.0855E+00	
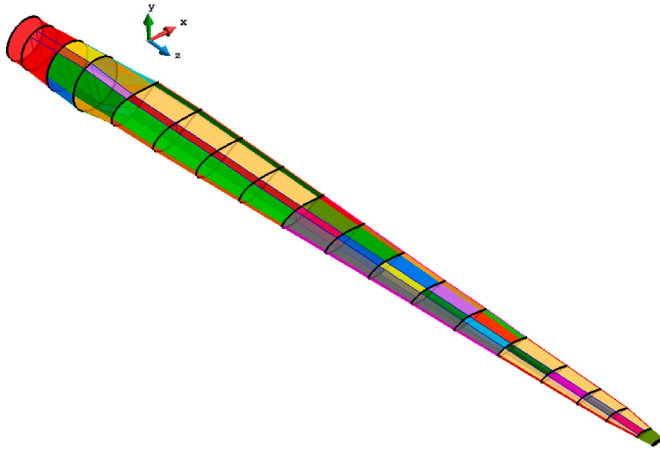
Fig. 3. The geometry of the blade from NuMAD.

FEM analysis.

First of all, the blade is divided into 18 sections and 19 stations. For each station, there is a chord length (c), a twist angle (θ_t), a blade span (L_{bs}), and an airfoil table specifically defined. Detailed data can be obtained from (Jonkman et al., 2009; Berg and Resor, 2012). Different from the original reports, several interp-sections were ignored to reduce the complexity of the FEM model. The parameters of each station of the blade are shown in Table 1.

The information about the airfoil tables is given in (Timmer and Van Rooij, 2003; Schweigler, 2012). The initial pitch angle (θ_p) was defined as 0° and when the wind speed exceeds the rated wind velocity, the pitch angle is applied correspondingly.

After creating the stations, the material properties of each station were specified by defining material division points. The blade consists of six different types of materials, which are Gelcoat, E-LT-5500 (UD), SNL (Triax), Saertex (DB), and Foam and Carbon (UD). Gelcoat and Foam can be treated as isotropic materials and the remaining ones are regarded as orthotropic materials. Material properties, including the composition of these materials in each section, can be obtained from (Resor, 2013; Griffith, 2013a, 2013b). Shear webs are significant and critical components for the blades because they reinforce the strength of the whole blade and make the blade more resistant to bending loadings. For this particular type of blade, the webs are located from 1.3667 m spans to

60.133 m spans and they are made from a combination of Saertex (DB) and Foam. The geometry of the final model in NuMAD is given in Fig. 3.

3.2. Loading calculation

For the current analysis, three types of loadings were considered including gravity, centrifugal force, and aerodynamic force. For gravity, since the density of the material is defined during the process of model generation, gravity can be applied as acceleration in ANSYS. The basic information about the speeds of the wind and the rotor is given in Table 2 (Jonkman et al., 2009).

The turbine is only in service when the wind velocity is between 3 m/s and 25 m/s. Otherwise, the rotor will be transformed to be parallel to the wind direction by the yaw control system. For the current analysis, the wind velocity is chosen as 6 m/s and according to the diagrams of Jonkman et al. (2009), the blade tip ratio is decided as 8. The expression of the blade tip ratio is given as:

$$r_{bt} = \frac{\omega R \cos(\theta_c)}{V_w} \tag{5}$$

where V_w is the wind velocity, ω is the angular velocity of the blade, and R is the length from the center of the rotor to the tip of the blade.

By using Eq. (6), the angular velocity of the blade can be determined as 7.28 rpm. The centrifugal force can also be applied in the format of acceleration:

$$a_c = \omega^2 r \tag{6}$$

where r is the distance from the middle of each section to the center of the rotor.

For the aerodynamic force, the blade element momentum theory (BEMT) was utilized. Although CFD simulation can usually perform more accurate aerodynamic analysis for the blades, CFD is very complex and time-consuming. Moreover, BEMT has been used and is still under-derutilization for the aerodynamic force calculation of blades (Zhang, 2018; Jureczko et al., 2005; Wen et al., 2017; Wang et al., 2014; Dai et al., 2011; Bavanish and Thyagarajan, 2013). For engineering analysis, BEMT is one of the simplest and most effective ways for wind force calculation (Zhang, 2018). The process of the BEMT application can be simplified as the following steps (Zhang, 2018).

1. Set the initial values of the axial and tangential induction factors (i_a and i_t) to 0;
2. The flow angle θ_f can be calculated by the following equation:

$$\theta_f = \tan^{-1}\left(\frac{(1-i_a)V_w}{(1+i_t)\omega r}\right) \tag{7}$$

3. By subtracting the twist angle (θ_t) and pitch angle (θ_p, currently equals 0), the attacking angle (θ_a) can be obtained:

$$\theta_a = \theta_f - \theta_t - \theta_p \tag{8}$$

4. With the help of the attacking angle, the coefficients for lift force (C_l), drag force (C_d), and pitching moment (C_m) can be obtained from the available data table (Zhang, 2018).
5. The method of Shen et al. (2005) for the tip and hub loss factors calculation is chosen here because they are more reliable after considering the experimental data.

$$g = e^{-0.125(N_b r_{bt} - 21)} + 0.1 \tag{9}$$

where N_b is the number of blades, $N_b = 3$.

The tip and hub loss factor can be calculated by the functions given below:

$$f_{tip} = \frac{2}{\pi}\cos^{-1}\left(e^{-g\frac{B(R-r)}{2r\,\sin(\theta_f)}}\right) \tag{10a}$$

$$f_{hub} = \frac{2}{\pi}\cos^{-1}\left(e^{-g\frac{B(r-r_{hub})}{2r_{hub}\,\sin(\theta_f)}}\right) \tag{10b}$$

The final total loss correction factor can be computed by multiplying f_{tip} with f_{hub}:

$$f_{lc} = f_{tip}f_{hub} \tag{11}$$

6. A pair of new induction factors can be calculated by the following expressions:

$$i'_a = \frac{1}{\frac{4f_{lc}\,\sin^2(\theta_f)}{r_s\,\cos^2(\theta_c)\left(C_l\,\cos(\theta_f)+C_d\,\sin(\theta_f)\right)}+1} \tag{12a}$$

$$i'_t = \frac{1}{\frac{4f_{lc}\,\sin(\theta_f)\cos(\theta_f)}{r_s\,\cos^2(\theta_c)\left(C_l\,\sin(\theta_f)-C_d\,\cos(\theta_f)\right)}-1} \tag{12b}$$

where r_s is the solidity ratio and it is defined as $r_s = \frac{N_b c}{2\pi r\cos(\theta_c)}$.

7. Comparing the new induction factors against the previous values, if the percentages of the differences are within 1%, the process will be completed. Otherwise, the process will return to the first step and the induction factors will be set as the average values of the newly calculated and previous induction factors. Repeat the whole process until the values are under the tolerance value.

8. Afterward, the relative wind velocity can be computed by the combination of the wind velocity and angular rotation speed as:

$$V_r = \sqrt{\left(V_w(1-i_a)\cos(\theta_c)\right)^2 + \left(\omega r(1+i_t)\cos(\theta_c)\right)^2} \tag{13}$$

9. The lift force (F_l), drag force (F_d), and pitching moment (M_p) for each section can be obtained based on the equations below:

$$F_l = \frac{1}{2}\rho_{air}cV_r^2C_ld_r \tag{14a}$$

$$F_d = \frac{1}{2}\rho_{air}cV_r^2C_dd_r \tag{14b}$$

$$M_p = \frac{1}{2}\rho_{air}c^2V_r^2C_md_r \tag{14c}$$

where ρ_{air} is the density of the air and 1.225 kg/m^3 is used and d_r is the length of each section.

By disassembling and reassembling these forces to the global coordinate system, the forces acting in the tangential and axial directions will be:

$$F_x = -F_l\,\sin(\theta_f) + F_d\,\cos(\theta_f) \tag{15a}$$

$$F_y = F_l\,\cos(\theta_f) + F_d\,\sin(\theta_f) \tag{15b}$$

$$M = M_p \tag{15c}$$

In order to check the accuracy of the force calculation, the total thrust force and torque are also calculated under the rated wind velocity condition by:

$$T = \sum_{i=1}^{n}\frac{1}{2}N_b\rho_{air}V_r^2\left(C_l\,\cos(\theta_f)+C_d\,\sin(\theta_f)\right)cd_r\,\cos(\theta_c) \tag{16a}$$
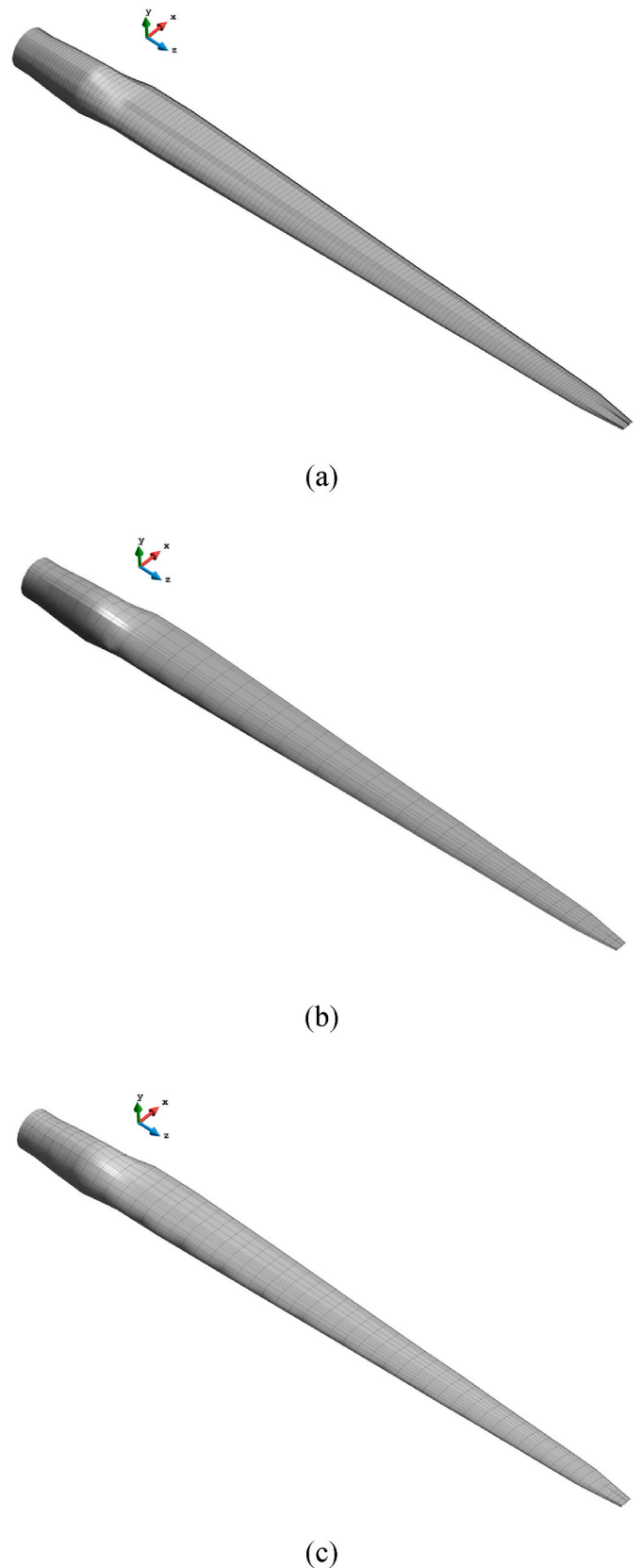

(a)

(b)

(c)

Fig. 4. The mesh for FEM (a), iFEM-972 (b), and iFEM-2070 (c) models.

Table 2

The velocities of wind and rotor.

	Wind Speed (m/s)	Rotor Speed (rpm)
Cut-In	3	6.9
Rated	11.4	12.1
Cut-Out	25	

Table 3

Comparison of results of FEM and iFEM analyses.

Cases	UT (m)	T (rad)
FEM (a)	2.596E+00	2.058E-01
iFEM-972 (b)	2.240E+00	2.757E-01
iFEM-2070 (c)	2.494E+00	1.976E-01
Differences between a & b	13.73%	33.95%
Differences between a & c	3.93%	3.98%

$$Q = \sum_{i=1}^{n} \frac{1}{2} N_b \rho_{air} V_r^2 \left(C_l \sin\left(\theta_f\right) - C_d \cos\left(\theta_f\right) \right) c d_r^2 \cos(\theta_c) \qquad (16b)$$

where n is the number of the sections. The calculated thrust force and torque are 734.91 kN and 4.33 MNm which are in the same range as the reference (Zhang, 2018). So, the process of force calculation can be verified.

By utilizing the same approach, the aerodynamic force when the wind velocity is 11.4 m/s can be calculated. For simplification of the FEM analysis, the tangential force is applied at the leading edge of each section (Yang and Baeder, 2016). However, the axial force and pitching moment were evenly applied to the nodes at the joint of the webs and bottom surface (Yang and Baeder, 2016). For the current analysis, the case that the blade is located horizontally and has a tendency of moving upward was selected. The root boundary of the blade was entirely fixed as the boundary condition. After applying the force to the FEM model, the reference results and strain data can be obtained for the following iFEM analysis.

3.3. Mesh generation and sensor selection

The model generated in NuMAD was exported for ANSYS. To avoid triangular elements, the model was re-meshed again with quadrilateral elements and finally, there are 18630 elements and 18457 nodes. Furthermore, an additional node was defined by using the Mass21 element type at the 61.5 m blade span together and making a rigid region to replace the closed-shell structure at the tip of the blade. The mesh of the FEM model is shown in Fig. 4(a) and for the whole analysis in this study the mesh for the FEM model will be kept unchanged to provide the reference solutions. It should be highlighted that the mesh size of the iFEM model will also have an impact on the results. For the general iFEM analysis, the iFEM element can be coarser and larger than the FEM element. The strain provider needs to be selected by the relative location of the element and usually, the central one would be a

reasonable choice. Otherwise, the sensor selection procedure will become complex and the accuracy of the analysis will also be reduced. At the same time, another aspect that needs to be considered for the iFEM model is to control the number of the iFEM elements and by doing so it can make a contribution to reduce the required number of sensors. This is always one of the major tasks of the iFEM analysis, i.e., the mesh size of the iFEM model should be relatively small to reduce the number of sensors.

For this study, the blade was modeled with a much coarser mesh and after balancing the requirements of fulfilling the completeness of the blade and reducing the number of the sensors, the number of elements becomes 2070 (see Fig. 4(c)). As shown in Table 2 and 3, 2070 element iFEM case provides more accurate results with respect to a coarser iFEM case with 972 elements (see Fig. 4(b)) when the blade is working under the rated wind velocity. The error is less than 4% for both displacement and rotation for the iFEM case with 2070 elements. Due to the fact that 2070 mesh size is more accurate, hence, it will be utilized during the following static and dynamic analyses as the full-sensor condition.

By logical selection of the FEM elements based on their relative positions, each iFEM element has a specific FEM element to offer the strain data for full-sensor conditions. Moreover, attention was also given to the reduction of the required number of sensors. For a blade, the root and tip are usually important regions. Additionally, there are some sharp changes in the zones between different airfoil shapes, especially between the circular station and the DU99-W-405 airfoil station. Therefore, sensors were placed at the back of this region to monitor large rotations of the blade. Since the length of the blade is much larger than the size of the cross-section, the top and bottom surfaces experience similar deformations, so the majority of the remaining sensors were installed only on the top surface. A line of sensors in the longitudinal span direction was chosen to keep the continuity of the analysis and a shorter line of sensors at the back surface of the blade was preferred. This can help to improve the monitoring of the condition of the leading edge around the tip region. Moreover, this will also strengthen the monitoring of the extreme flap-wise displacements which are usually the most severe deformations suffered by the blades. After testing the accuracy of different distributions of these sensors, 147 sensor locations were selected and the locations of these sensors are shown in Fig. 5.

Therefore, during the iFEM analysis, only 147 locations were installed with sensors for the reduced-sensor condition, i.e. only 147 iFEM elements can obtain the input strain data. With the help of FBG technology, the sensors can be installed with only 6 × 2 cables. By analyzing the frequency interval, the strain data can be separated into normal and in-plane shear strains, and then they can be inputted into iFEM analysis.

3.4. Results for static condition

For the deformation of a blade, the flap-wise displacements are always more severe than the others. In the current coordinate system, the displacements in the y-direction are the dominant ones and according to the FEM results, they would be around 10 times larger than the U and W
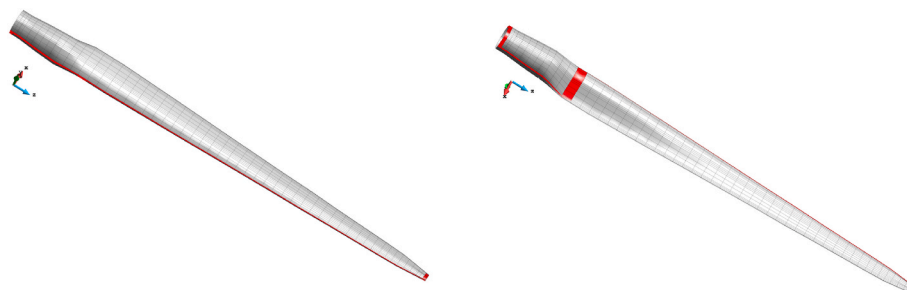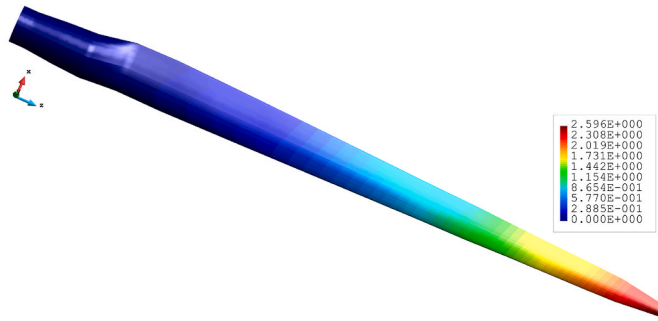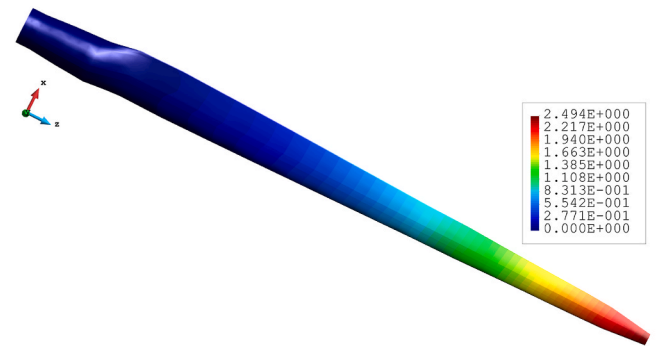

Fig. 5. The selected sensor locations for iFEM analysis.

Table 4

The results of FEM and iFEM analysis.

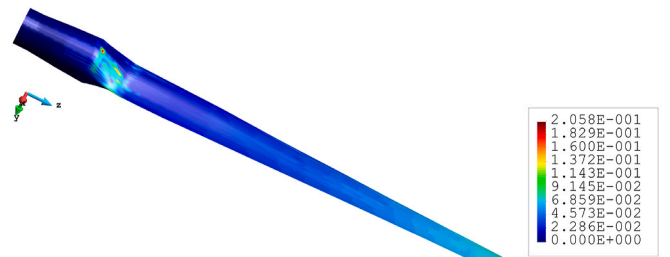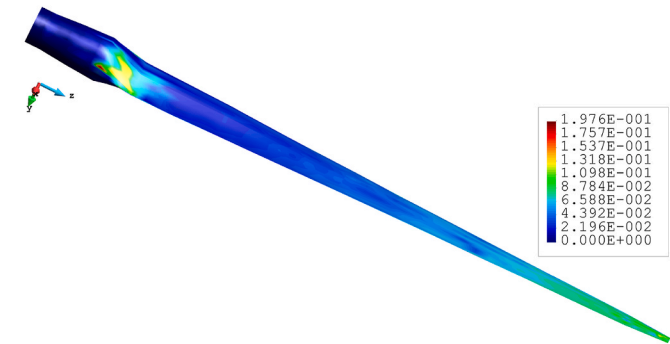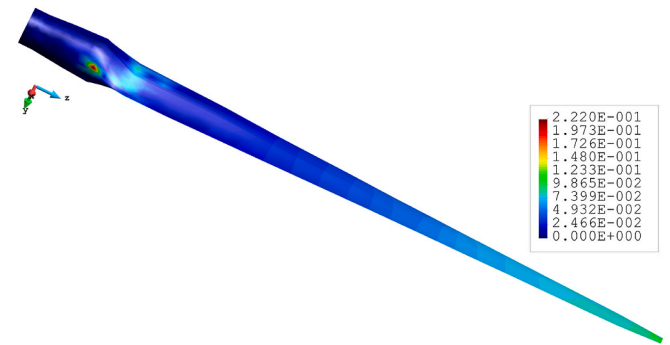| Cases	UT (m)	T (rad)
FEM (a)	2.596E+00	2.058E-01
iFEM (b)	2.494E+00	1.976E-01
iFEM-147 (c)	2.563E+00	2.220E-01
Differences between a & b	3.93%	3.98%
Differences between a & c	1.27%	7.87%

(a) FEM

(b) iFEM
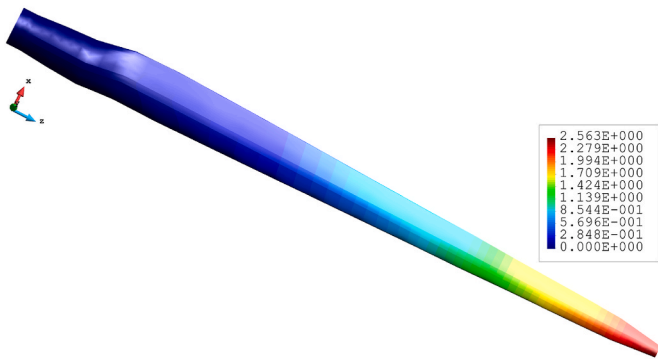
(c) iFEM-147

Fig. 6. The plots of the total displacements (*m*).

(a) FEM

(b) iFEM

(c) iFEM-147

Fig. 7. The plots of the total rotations (*rad*).

displacements. In order to clearly and concisely represent the displacement field, total displacements are selected. For the full-sensor condition, the maximum total displacements are estimated as 2.494 m and which is about 3.93% less than the reference result (2.596 m). But for the reduced sensor condition, the estimation of the extreme total displacements is improved and it is only about 1.27% over the reference value. On the other hand, as can be seen in Table 4, the iFEM with reduced sensors becomes less accurate than the full-sensor iFEM when evaluating the total rotations. iFEM with full sensors can obtain a
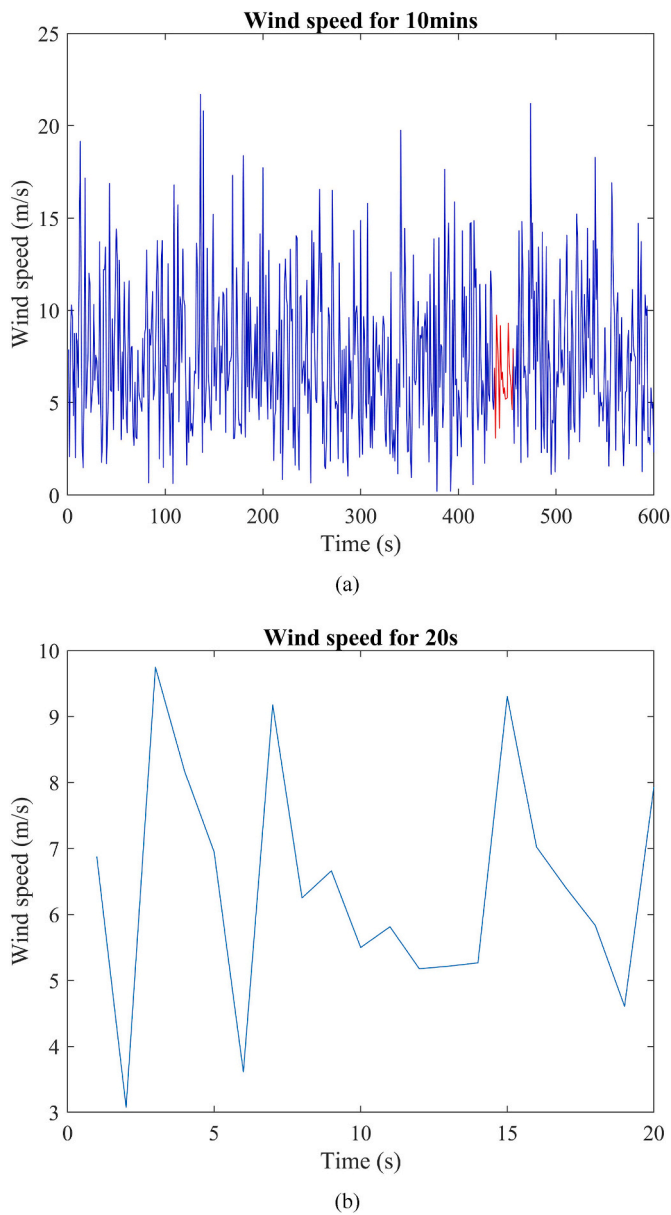
(a)

(b)

Fig. 8. Wind speed for 10 min (a) and selected 20 s (b).

(a)

(b)

Fig. 9. The results for the dynamic case, (a) total displacement and (b) total rotation.

maximum total rotation of 0.1976 *rad* which is just about 4% less than the reference value. Moreover, iFEM with reduced sensors obtain a value of 0.2220 *rad* as the extreme total rotations and it is approximately 8% higher than the FEM result. The reasons causing the relatively high percentage are, on the one hand, reducing the number of sensors will negatively influence the accuracy. On the other hand, usually, the maximum value of the total rotations concentrates in a limited region.

The variation of the total displacements and total rotations are also given to enhance the explanation of the results of iFEM (Figs. 6 and 7). For the total displacements, it can be seen that for all three plots, the displacements are smoothly distributed along the span of the blade. The differences between these three plots are indistinguishable which proves that the iFEM results no matter with full sensors or reduced sensors are in good agreement with the reference FEM results. In terms of total rotations, the maximum value concentrates on the transition region of the blade and this feature can be accurately captured by iFEM with full sensors. However, with the reduction of the sensors, there will not be any sensors placed in the region that contains the information on the maximum total rotations. The value can only be approached by the iFEM
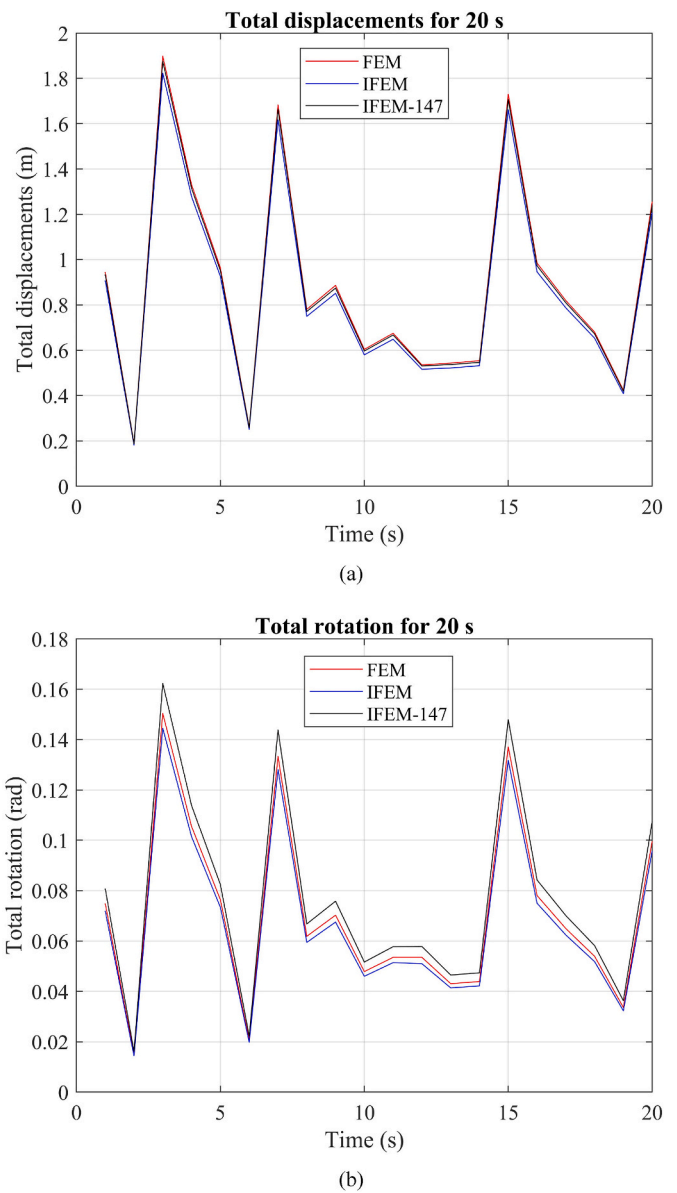
elements with sensors, near this region. So it is not surprising that the maximum total rotation occurs in the iFEM elements with sensors, which are located around the transition zone.

3.5. Results for the dynamic condition with various wind velocities

For the dynamic case, different wind speeds are taken into consideration. The wind speed data is generated by Rayleigh Distribution, which is a simplified format of Weibull Distribution, for 10 min (Fig. 8 (a)). For each second there is a specific wind speed, but only 20 s (red region in Fig. 8(a) and shown in Fig. 8(b)) are selected for the analysis. The wind force is calculated following the previously mentioned BEMT method, and the gravity and centrifugal forces are still kept during the analysis.

The dynamic analysis for both the full-sensor condition and reduced-sensor condition is performed and the sensor locations are kept the same as in the static case. The maximum total displacements and total rotations are recorded for each time step and the results are plotted in Fig. 9. In order to further illustrate the results, the percentages of the difference
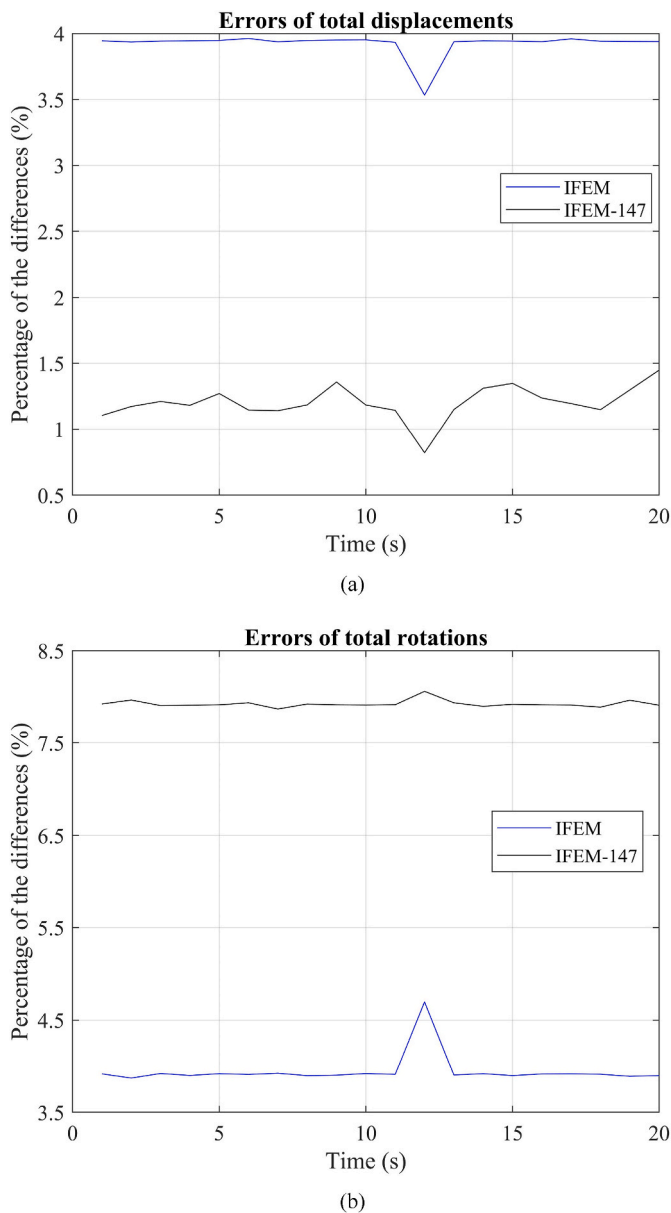
Fig. 10. The errors for the dynamic case, (a) total displacement and (b) total rotation.

of the iFEM results against reference results are also provided (Fig. 10). First of all, for the total displacements, the results from iFEM analysis for 20 s match well with the FEM results. Moreover, the figures of the errors also support this observation. The percentages of the difference are all less than 5%. For the full-sensor condition, the values range between 3.5% and 4%. For the iFEM with just 147 sensors, the accuracy becomes even better with just around 1.5% differences. When it comes to rotation, it becomes rather different. For full-sensor iFEM, the results are slightly underestimated but the results are still with high accuracy with errors of less than 5%. However, for the 147-sensors case, similar to the static case, the values are stable at around 8%. The reasons are expected the same as in the static case. Since the errors are less than 10% together with the practical number of sensors, the results can be recognised as reasonable. Finally, the aim of monitoring the composite blade is successfully achieved.

4. Conclusions

In this study, shape sensing of the blade of the NREL 5 MW offshore wind turbine is demonstrated by using the iFEM method. The real loading conditions are considered during both the static and dynamic analyses. The analysis of FEM is used as a reference solution for the iFEM analysis and it also provides the strain data for the iQS4 elements. After comparing the results of iFEM with the FEM results, it can be concluded that iFEM can obtain an accurate real-time 3-D displacement field for the blade even with the suggested practical numbers of sensors, which is only 147 × 2 sensors and can be replaced by 6 × 2 cables of FBG sensors. It can also be concluded that the iQS4 element has the ability to monitor offshore wind turbine blades.

CRediT authorship contribution statement

Mingyang Li: Conceptualization, Methodology, Software, Writing – original draft. **Yildirim Dirik:** Methodology, Software. **Erkan Oterkus:** Conceptualization, Methodology, Supervision, Writing – review & editing. **Selda Oterkus:** Supervision.

Declaration of competing interest

The authors declare that they have no known competing financial interests or personal relationships that could have appeared to influence the work reported in this paper.

Data availability

Data will be made available on request.

References

Albanesi, A., Fachinotti, V., Peralta, I., Storti, B., Gebhardt, C., 2017. Application of the inverse finite element method to design wind turbine blades. Compos. Struct. 161, 160–172.

Albanesi, A., Bre, F., Fachinotti, V., Gebhardt, C., 2018. Simultaneous ply-order, ply-number and ply-drop optimization of laminate wind turbine blades using the inverse finite element method. Compos. Struct. 184, 894–903.

Antoniadou, I., Dervilis, N., Papatheou, E., Maguire, A.E., Worden, K., 2015. Aspects of structural health and condition monitoring of offshore wind turbines. Phil. Trans. Math. Phys. Eng. Sci. 373 (2035), 20140075.

Arsenault, T.J., Achuthan, A., Marzocca, P., Grappasonni, C., Coppotelli, G., 2013. Development of a FBG based distributed strain sensor system for wind turbine structural health monitoring. Smart Mater. Struct. 22 (7), 075027.

Bavanish, B., Thyagarajan, K., 2013. Optimization of power coefficient on a horizontal axis wind turbine using bem theory. Renew. Sustain. Energy Rev. 26, 169–182.

Berg, J.C., Resor, B.R., 2012. Numerical Manufacturing and Design Tool (NuMAD V2. 0) for Wind Turbine Blades: User's Guide. Sandia National Laboratories Technical Report. *SAND2012-7028*.

Cerracchio, P., Gherlone, M., Di Sciuva, M., Tessler, A., 2015. A novel approach for displacement and stress monitoring of sandwich structures based on the inverse Finite Element Method. Compos. Struct. 127, 69–76.

Ciang, C.C., Lee, J.R., Bang, H.J., 2008. Structural health monitoring for a wind turbine system: a review of damage detection methods. Meas. Sci. Technol. 19 (12), 122001.

Colombo, L., Sbarufatti, C., Giglio, M., 2019. Definition of a load adaptive baseline by inverse finite element method for structural damage identification. Mech. Syst. Signal Process. 120, 584–607.

Dai, J.C., Hu, Y.P., Liu, D.S., Long, X., 2011. Aerodynamic loads calculation and analysis for large scale wind turbine based on combining BEM modified theory with dynamic stall model. Renew. Energy 36 (3), 1095–1104.

Fachinotti, V.D., Cardona, A., Jetteur, P., 2008. Finite element modelling of inverse design problems in large deformations anisotropic hyperelasticity. Int. J. Numer. Methods Eng. 74 (6), 894–910.

Fachinotti, V.D., Albanesi, A.E., Valle, J.M.M., 2015. Inverse finite element modeling of shells using the degenerate solid approach. Comput. Struct. 157, 89–98.

Fernandez, G., Usabiaga, H., Vandepitte, D., 2018. An efficient procedure for the calculation of the stress distribution in a wind turbine blade under aerodynamic loads. J. Wind Eng. Ind. Aerod. 172, 42–54.

Gherlone, M., Cerracchio, P., Mattone, M., Di Sciuva, M., Tessler, A., 2012. Shape sensing of 3D frame structures using an inverse finite element method. Int. J. Solid Struct. 49 (22), 3100–3112.

Gherlone, M., Cerracchio, P., Mattone, M., Di Sciuva, M., Tessler, A., 2014. An inverse finite element method for beam shape sensing: theoretical framework and experimental validation. Smart Mater. Struct. 23 (4), 045027.

Griffith, D.T., 2013a. The SNL100-01 Blade: Carbon Design Studies for the Sandia 100-meter Blade. Sandia National Laboratories Technical Report. *SAND2013-1178*.

Griffith, D.T., 2013b. The SNL100-02 Blade: Advanced Core Material Design Studies for the Sandia 100-meter Blade. Sandia National Laboratories Technical Report. *SAND2013-10162*.

Hsu, M.C., Akkerman, I., Bazilevs, Y., 2014. Finite element simulation of wind turbine aerodynamics: validation study using NREL Phase VI experiment. Wind Energy 17 (3), 461–481.

Jonkman, J., Butterfield, S., Musial, W., Scott, G., 2009. *Definition of a 5-MW Reference Wind Turbine for Offshore System development*(No. NREL/TP-500-38060). National Renewable Energy Lab.(NREL), Golden, CO (United States).

Joosse, P.A., Blanch, M.J., Dutton, A.G., Kouroussis, D.A., Philippidis, T.P., Vionis, P.S., 2002. Acoustic emission monitoring of small wind turbine blades. J. Sol. Energy Eng. 124 (4), 446–454.

Jureczko, M.E.Z.Y.K., Pawlak, M., Mężyk, A., 2005. Optimisation of wind turbine blades. J. Mater. Process. Technol. 167 (2–3), 463–471.

Kefal, A., 2017. Structural Health Monitoring of Marine Structures by Using Inverse Finite Element Method. Doctoral dissertation, University of Strathclyde.

Kefal, A., Oterkus, E., 2016a. Displacement and stress monitoring of a chemical tanker based on inverse finite element method. Ocean Eng. 112, 33–46.

Kefal, A., Oterkus, E., 2016b. Displacement and stress monitoring of a Panamax containership using inverse finite element method. Ocean Eng. 119, 16–29.

Kefal, A., Yildiz, M., 2017. Modeling of sensor placement strategy for shape sensing and structural health monitoring of a wing-shaped sandwich panel using inverse finite element method. Sensors 17 (12), 2775.

Kefal, A., Oterkus, E., Tessler, A., Spangler, J.L., 2016. A quadrilateral inverse-shell element with drilling degrees of freedom for shape sensing and structural health monitoring. Eng. sci. technol. int. j. 19 (3), 1299–1313.

Kefal, A., Tessler, A., Oterkus, E., 2017. An enhanced inverse finite element method for displacement and stress monitoring of multilayered composite and sandwich structures. Compos. Struct. 179, 514–540.

Kefal, A., Mayang, J.B., Oterkus, E., Yildiz, M., 2018. Three dimensional shape and stress monitoring of bulk carriers based on iFEM methodology. Ocean Eng. 147, 256–267.

Kim, S.W., Kang, W.R., Jeong, M.S., Lee, I., Kwon, I.B., 2013. Deflection estimation of a wind turbine blade using FBG sensors embedded in the blade bonding line. Smart Mater. Struct. 22 (12), 125004.

Kim, H.C., Kim, M.H., Choe, D.E., 2019. Structural health monitoring of towers and blades for floating offshore wind turbines using operational modal analysis and modal properties with numerical-sensor signals. Ocean Eng. 188, 106226.

Li, M.Y., Kefal, A., Cerik, B., Oterkus, E., 2019. Structural health monitoring of submarine pressure hull using inverse finite element method. In: Trends in the Analysis and D*esign of Marine Structures: Proceedings of the 7th International Conference on Marine Structures (MARSTRUCT 2019, Dubrovnik, Croatia, 6-8 May 2019)*. CRC Press, p. 293.

Li, M., Kefal, A., Cerik, B.C., Oterkus, E., 2020. Dent damage identification in stiffened cylindrical structures using inverse Finite Element Method. Ocean Eng. 198, 106944.

Resor, B.R., 2013. Definition of a 5MW/61.5 M Wind Turbine Blade Reference Model. Sandia National Laboratories, Albuquerque, New Mexico, USA. *SAND2013-2569*, 2013.

Schubel, P.J., Crossley, R.J., Boateng, E.K.G., Hutchinson, J.R., 2013. Review of structural health and cure monitoring techniques for large wind turbine blades. Renew. Energy 51, 113–123.

Schweigler, K., 2012. *Aerodynamic analysis of the Nrel 5-mw Wind Turbine Using Vortex Panel method*(Master's Thesis).

Shen, W.Z., Mikkelsen, R., Sørensen, J.N., Bak, C., 2005. Tip loss corrections for wind turbine computations. Wind Energy: An Int. J. Progr. Appl. Wind Power Convers. Technol. 8 (4), 457–475.

Swartz, R.A., Lynch, J.P., Zerbst, S., Sweetman, B., Rolfes, R., 2010. Structural monitoring of wind turbines using wireless sensor networks. Smart Struct. Syst. 6 (3), 183–196.

Tessler, A., Spangler, J.L., 2003. A Variational Principle for Reconstruction of Elastic Deformations in Shear Deformable Plates and Shells.

Tessler, A., Spangler, J.L., 2004. Inverse FEM for Full-Field Reconstruction of Elastic Deformations in Shear Deformable Plates and Shells.

Tian, S., Yang, Z., Chen, X., Xie, Y., 2015. Damage detection based on static strain responses using FBG in a wind turbine blade. Sensors 15 (8), 19992–20005.

Timmer, W.A., Van Rooij, R.P.J.O.M., 2003. Summary of the Delft University wind turbine dedicated airfoils. J. Sol. Energy Eng. 125 (4), 488–496.

Wang, L., Liu, X., Renevier, N., Stables, M., Hall, G.M., 2014. Nonlinear aeroelastic modelling for wind turbine blades based on blade element momentum theory and geometrically exact beam theory. Energy 76, 487–501.

Wen, B., Wei, S., Wei, K., Yang, W., Peng, Z., Chu, F., 2017. Power fluctuation and power loss of wind turbines due to wind shear and tower shadow. Front. Mech. Eng. 12 (3), 321–332.

Yang, S.J., Baeder, J.D., 2016. Effect of wavy trailing edge on 100meter flatback wind turbine blade. In: Journal of Physics: Conference Series, vol. 753. *IO*P Publishing. No. 2, p. 022060.

Yang, W., Tavner, P.J., Crabtree, C.J., Feng, Y., Qiu, Y., 2014. Wind turbine condition monitoring: technical and commercial challenges. Wind Energy 17 (5), 673–693.

Zhang, C., 2018. Reliability-based Fatigue Damage Assessment and Optimum Maintenance Strategy of Offshore Horizontal Wind Turbine Blades. Doctoral dissertation, University of Greenwich.

Zhang, C., Chen, H.P., Huang, T.L., 2018. Fatigue damage assessment of wind turbine composite blades using corrected blade element momentum theory. Measurement 129, 102–111.